

A flat inner disc model as an alternative to the Kepler dichotomy in the Q1–Q16 planet population

T. Bovaird^{1,2★} and C. H. Lineweaver^{1,2,3★}

¹Research School of Astronomy and Astrophysics, Australian National University, Canberra, ACT 2611, Australia

²Planetary Science Institute, Australian National University, Canberra, ACT 2611, Australia

³Research School of Earth Sciences, Australian National University, Canberra, ACT 2611, Australia

Accepted 2017 February 15. Received 2017 February 10; in original form 2016 August 21

ABSTRACT

We use simulated planetary systems to model the planet multiplicity of Kepler stars. Previous studies have underproduced single planet systems and invoked the so-called Kepler dichotomy, where the planet forming ability of a Kepler star is dichotomous, producing either few or many transiting planets. In this paper, we show that the Kepler dichotomy is only required when the inner part of planetary discs are just assumed to be flared. When the inner part of planetary discs are flat, we reproduce the observed planet multiplicity of Kepler stars without the need to invoke a dichotomy. We find that independent of the disc model assumed, the mean number of planets per star $\mu \approx 2$ for orbital periods between 3 and 200 d, and for planetary radii between 1 and 5 Earth radii. This contrasts with the Solar system where no planets occupy the same parameter space.

Key words: protoplanetary discs – planetary systems.

1 INTRODUCTION

The Kepler Q1–Q16 catalogue (Mullally et al. 2015) uses 47 months of Kepler data collected from $\sim 190\,000$ stars. This has resulted in the detection of over 4000 planet candidates orbiting ~ 3200 stars. While the majority of the ~ 3200 stars contain a single detected planet, transit signals from multiple planets have been detected around 656 of these stars. Comparisons to the architecture of the Solar system are limited, due to the relatively smaller periods and planetary radii that Kepler can efficiently sample.

1.1 The Kepler dichotomy

The mutual inclination distribution between planets around Kepler stars has been well studied (Lissauer et al. 2011; Fang & Margot 2012; Figueira et al. 2012; Johansen et al. 2012; Tremaine & Dong 2012; Weissbein, Steinberg & Sari 2012; Fabrycky et al. 2014; Ballard & Johnson 2016, see Appendix E). The majority of these studies show good agreement between simulated planets and the Kepler sample when the orbital planes of simulated planets are closely aligned. Specifically, when the mutual inclinations between planets are drawn from a Rayleigh distribution (a ‘flared’ planetary disc) with a mode of the flare angle between $\sim 1^\circ$ and 5° .

In contrast to the agreement for mutual inclinations, some studies report a significant underproduction of simulated systems with a single detected planet (Lissauer et al. 2011; Johansen et al. 2012;

Hansen & Murray 2013; Ballard & Johnson 2016). These studies underproduce the number of simulated stars with a single detected transiting planet by a factor of ~ 3 .

The underproduction of simulated systems with a single detected transiting planet has led to the proposal of dichotomous planetary systems in the Kepler field, the so-called Kepler Dichotomy. One population of planetary systems is required to either suppress planet formation, or be ‘dynamically hot’ (Hansen & Murray 2013), where mutual inclinations between planets are increased, or where planets are more likely to be ejected from the system. For the host stars in these planetary systems, the probability of detecting multiple transiting planets is reduced, leading to a higher proportion of stars with a single detected transiting planet in this population.

Potential explanations for the dynamically hot planetary system population include dynamical instability caused by high-mass planets (Johansen et al. 2012; Lai & Pu 2017), instability or suppressed planet formation caused by stellar binaries (Ballard & Johnson 2016), varying surface density profiles and disc masses (Moriarty & Ballard 2016), varying strengths of gas depletion or spin-orbit misalignment between the star and planet (Spalding & Batygin 2016). Ballard & Johnson (2016) show that to account for the excess of detected single-planet transiting systems around M dwarfs, these stars with a reduced probability of multiple transiting planets need to account for ~ 55 per cent of M dwarfs in the Kepler field.

1.2 Detected transiting planets

We define the true planetary system multiplicity vector N_k as the number of stars that are host to k planets. For the Kepler mission

* E-mail: timothy.bovaird@anu.edu.au (TB); charley.lineweaver@anu.edu.au (CHL)

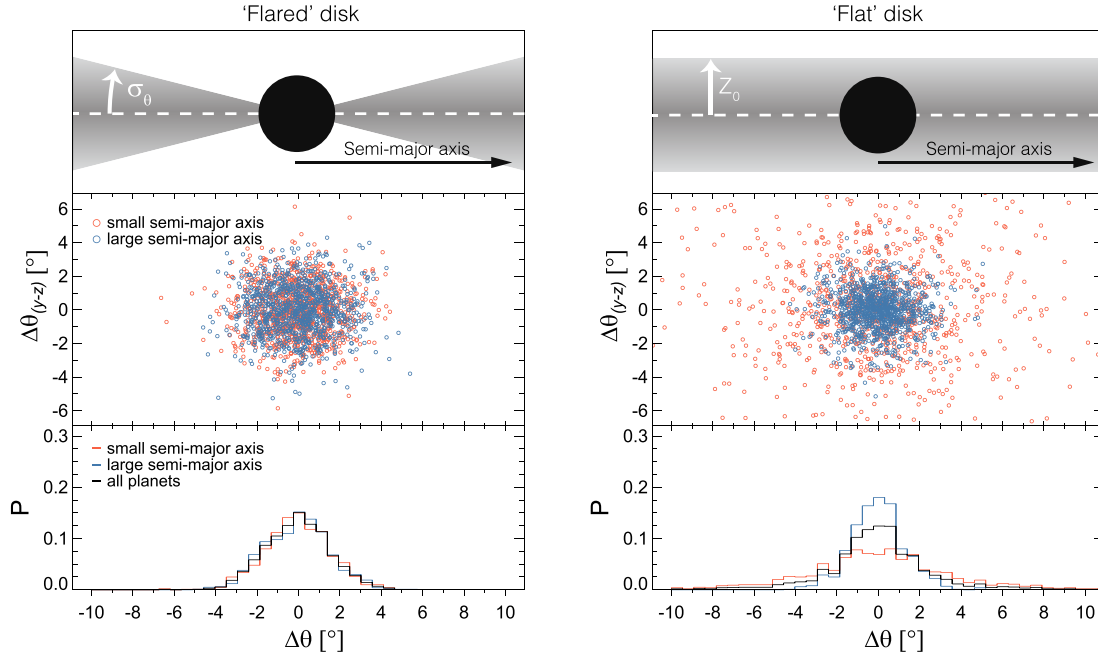


Figure 1. Comparing the two disc models from Section 1.4, a ‘flared’ (left) and ‘flat’ (right) disc. The top panels illustrate the two models viewed edge-on, i.e. perpendicular to the invariable plane (indicated by the white dashed line). The simulated inclinations (see Fig. A1) of planets with small (0.05–0.3 au, red) and large (0.3–0.6 au, blue) semimajor axes (around a Solar mass star) are shown in the middle panel for each model. Under the flared disc model, the distribution of inclinations is independent of semimajor axis, whereas under the flat disc model, planets with a smaller semimajor axis tend to have a larger inclination and vice versa. The bottom panel displays the distribution for the one component of inclination that the transit method is sensitive to (Section 1.3 and Fig. A1).

(and any transit survey), the observed vector \hat{N}_k will be significantly lower than the true N_k , due to the low probability of planets transiting their host star, and since Kepler can only efficiently detect planets across a small fraction of parameter space. The observed planetary system multiplicity vector, hereafter simply referred to as the multiplicity vector, is given by

$$\hat{N}_k = [\hat{N}_1, \hat{N}_2, \hat{N}_3, \dots], \quad (1)$$

where \hat{N}_1 , \hat{N}_2 and \hat{N}_3 are the number of stars with 1, 2 and 3 *detected* transiting planets, respectively, and so on. For the Kepler Q1–Q16 catalogue (see Section 2.1), $1 \leq k \leq 6$ and $\hat{N}_k = [2608, 413, 141, 52, 18, 3]$.

1.3 Mutual inclinations

For two or more planets in the same planetary system, the mutual inclination between those planets is defined as the angle between their orbital planes. The probability of multiple planets transiting the same star is non-negligible for small mutual inclinations only, generally of the order of a few degrees. Planets in the system with larger mutual inclinations, relative to the transiting planets, require alternative detection methods.

In general, the true inclination of the orbital plane of a transiting planet cannot be determined from a transit light curve alone. The transit method is only sensitive to the line-of-sight component of the inclination i (Fig. A1). In Fig. 1, the distribution of the detectable inclination component for a set of simulated planets is shown in the bottom panels. The orthogonal component of inclination, typically not detectable by the transit method, represents the y -axis of the middle panels. The true mutual inclination between a pair of planets is given by $\sqrt{\Delta\theta^2 + \Delta\theta_{(y-z)}^2}$.

1.4 An alternative disc model

In the studies mentioned in Section 1.1, the true mutual inclinations between simulated planets are drawn from a Rayleigh distribution with mode $\sigma_{\Delta\phi}$. The Rayleigh distribution is composed of two Gaussian distributed components, with standard deviations equal to $\sigma_{\Delta\phi}$. We can visualize the inclination distribution by considering one of these Gaussian components, i.e. viewing systems edge-on at an arbitrary plane perpendicular to the invariable plane, as in the top panels of Fig. 1. Rayleigh distributed mutual inclinations represent a ‘flared disc’ model, where a planet’s height above the invariable plane¹ tends to increase with increasing semimajor axis. Planet inclinations relative to the invariable plane do not depend on semimajor axis.

In this paper, we use a ‘flat disc’ model, where a planet’s height above the invariable plane does not depend on semimajor axis, and planet inclinations relative to the invariable plane tend to decrease with increasing semimajor axis (as seen in the right-hand panels of Fig. 1). Hansen & Murray (2013) tested the *in situ* assembly of close in planets, and found that planets with small semimajor axes tended to have larger inclinations, particularly <0.1 au.

We apply this flat disc model to the typical semimajor axis space probed by Kepler, i.e. the interior part of planetary discs, as shown in Fig. 2. In general, this represents planets with semimajor axes much less than the semimajor axes of the inner Solar system planets. We improve on previous modelling efforts by removing the flared disc assumption. We show that for a flat inner planetary disc there is no need to invoke a dichotomous planetary system population,

¹ The mode of the Rayleigh distribution of inclinations relative to an invariable plane σ_ϕ , is related to the Rayleigh distribution of mutual inclinations $\sigma_{\Delta\phi}$, by $\sigma_\phi \approx \sigma_{\Delta\phi}/\sqrt{2}$.

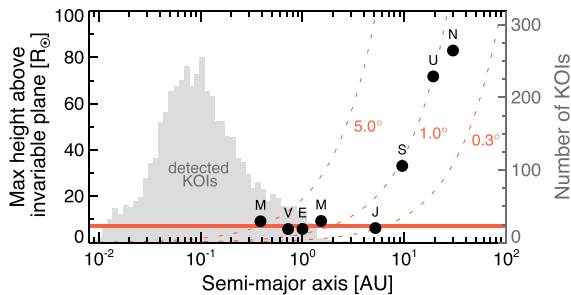


Figure 2. The maximum height above the Solar system’s invariable plane over a single orbit for Solar system planets. Interior to Jupiter, the height above the invariable plane is approximately constant, represented by the red line with a value $Z_{\max} \approx 8 R_{\odot}$. Exterior to Jupiter, the height above the invariable plane flares out with increasing semimajor axis. Dashed lines of constant inclination relative to the invariable plane, are shown for 0.3° , 1° and 5° . The semimajor axis distribution of Kepler Q1–Q16 planet candidates (grey histogram) falls well within the Solar system’s constant-height regime.

where one population of host stars have a decreased probability of hosting multiple transiting planets.

In Section 2, we define our stellar and planetary samples, based on minimizing false positives and false negatives. In Section 3, we estimate the transit and detection completeness across our parameter space. In Section 4, we estimate the underlying orbital period and planet radius distributions. We outline the process of producing model planetary populations in Section 5. In Section 6, we compare the simulated detections in our model systems to the Kepler Q1–Q16 candidates, for both flat and flared disc models. In Section 7, we discuss the results from our model planet populations, including estimates for the mean number of planets per star within our parameter space.

2 SAMPLE SELECTION

When we generate a model planetary system, the stellar properties for that system are assigned from a random Kepler star in our stellar sample. We produce our input stellar sample in the following way.

We begin with the 198 917 stars from the Kepler Q16 stellar catalogue.² We limit our sample to low-noise Solar type stars, similar to the majority of previous studies mentioned in Section 1.1. We apply the following cuts to the input catalogue:

$$\begin{aligned}
 4100 \text{ K} < T_{\text{eff}} < 6100 \text{ K}, \\
 \sigma_{\text{CDPP}_{45}} < 200 \text{ ppm}, \\
 R_* < 1.15 R_{\odot}, \\
 T_{\text{baseline}} > 1000 \text{ d}, \\
 f_{\text{duty}} > 0.6,
 \end{aligned} \tag{2}$$

where T_{eff} and R_* are the stellar effective temperature and radius, respectively. The 4.5 h CDPP (combined differential photometric precision, Christiansen et al. 2012) of the star, a measure of the combined instrumental and stellar noise, is given by $\sigma_{\text{CDPP}_{45}}$. T_{baseline} is the timespan of observations for each star and f_{duty} is the fraction of valid observations over T_{baseline} . Note that the combination of $T_{\text{baseline}} > 1000 \text{ d}$ and $f_{\text{duty}} > 0.6$ generally ensures at least three transits for orbital periods up to 200 d.

The above stellar cuts, in addition to removing stars without a reported mass, result in our input stellar sample of 63 128 stars. In later sections, the stellar properties of each simulated planetary system are assigned from a randomly drawn star in this sample.

To minimize the detection incompleteness and false-positives in our observed planet sample, to which we will compare our simulations, we select only those planets with a high pipeline detection efficiency. We begin with the 1338 Kepler objects of interest (KOIs) labelled ‘candidate’ by the Q1–Q16 pipeline³. An additional 4401 KOIs are labelled ‘not dispositioned’. We update these dispositions using the Kepler Q17 catalogue for reference. This results in 2812 KOIs changing from ‘not dispositioned’ to ‘candidate’.

These planets form our initial sample of 4150 planet candidates from the Q1–Q16 catalogue (Mullally et al. 2015). To conform with our input stellar sample, we remove planets around host stars outside of our stellar parameter space defined by equation (2). This reduces our sample of observed planets from 4150 to 1790.

We set an upper orbital period limit of 200 d to avoid the increase in false-positives towards the Kepler orbital period of $\sim 372 \text{ d}$ (Mullally et al. 2015), and to remain consistent with the Kepler pipeline completeness calculations (Christiansen et al. 2015).

The Kepler pipeline is known to have an increasing false-negative rate with decreasing orbital period for orbital periods $\lesssim 3 \text{ d}$. This is largely due to the pipeline harmonic filter, which can remove transit signals that are on the same timeframe as the expected stellar noise (Christiansen et al. 2015). In addition, a small fraction of the fitted planetary radii for planets with orbital periods $\lesssim 10 \text{ d}$ can be significantly lower than the true planet radius, diluting the transit signals for some of these planets. We choose an orbital period lower limit of 3 d, in order to retain a sample of Kepler stars with ≥ 4 transiting planets.

The Kepler pipeline reports a summary statistic for the strength of a transit detection, the multiple event statistic (MES). A lower limit planet radius of $1 R_{\oplus}$ and a lower limit MES of 10 are chosen since false-positives are dominated by low MES ($\lesssim 8$) detections (Mullally et al. 2015). An upper planet radius limit of $5 R_{\oplus}$ is chosen to avoid increasing false-positives with planet size, and since the mass–radius relation becomes degenerate for larger planetary radii.

To summarize, we only retain the Kepler Q1–Q16 candidates that meet the following criteria:

$$\begin{aligned}
 3 \text{ d} < P < 200 \text{ d}, \\
 1 R_{\oplus} < R_p < 5 R_{\oplus}, \\
 \text{MES} > 10.
 \end{aligned} \tag{3}$$

This results in our observed sample of 1077 candidates in 816 planetary systems, within the parameter space outlined in equations (2) and (3). The observed planetary system multiplicity vector \hat{N}_k (equation 1) for our parameter space is given by

$$\hat{N}_k = [631, 127, 45, 9, 3, 1]. \tag{4}$$

3 TRANSIT AND DETECTION EFFICIENCY

When attempting to estimate the underlying multiplicity vector N_k given the observed \hat{N}_k (equation 1), there exists a degeneracy between the underlying multiplicity distribution and the underlying mutual inclination distribution. For example, an observed \hat{N}_k could be reproduced by systems that contain many planets with a large

² <http://exoplanetarchive.ipac.caltech.edu/cgi-bin/TblSearch/nph-tblSearchInit?app=ExoTbIs&config=keplerstellar>

³ <http://exoplanetarchive.ipac.caltech.edu/cgi-bin/TblView/nph-tblView?app=ExoTbIs&config=koi>

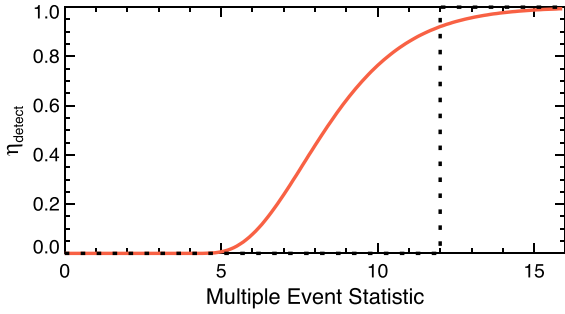


Figure 3. The Kepler Q1–Q16 pipeline detection completeness as a function of MES (equation 5), from Christiansen et al. (2015). The black dashed line represents a typical completeness step function assumed in previous studies. The full form of the pipeline detection completeness can be seen in equation (6).

dispersion in mutual inclinations, or by systems containing fewer planets but with a small mutual inclination dispersion. These two underlying distributions must be modelled simultaneously.

We estimate the underlying inclination and multiplicity distributions of Kepler systems in the Q1–Q16 catalogue, within the period and radius parameter space where Kepler can more reliably detect transiting planets (given by equations 2 and 3). We produce sets of 10^6 simulated planetary systems across a grid of inclination and multiplicity distributions. For each set of model assumptions, we estimate the probability of Kepler detecting each simulated planet. By comparing the \hat{N}_k for a set of simulated systems to the \hat{N}_k for the Q1–Q16 Kepler catalogue, we can estimate the underlying architecture between planetary orbital planes and the distribution of the number of planets per star.

3.1 Pipeline detection efficiency

Detection incompleteness and false-positives are important issues when comparing the detected planets around simulated and observed stars. Previous studies did not have the benefit of the Kepler pipeline detection completeness provided by transit injection and recovery experiments (Christiansen et al. 2015), shown in Fig. 3.

We follow the approximation of the pipeline MES by (Burke et al. 2015), which includes a limb-darkening approximation and accounts for non-zero impact parameters.

$$\text{MES} = \frac{0.84 \delta (c + s\sqrt{\delta})}{\sigma_{\text{cdpp}}} \sqrt{n_{\text{tr}}}, \quad (5)$$

where $c = 1.0874$ and $s = 1.0187$ for G dwarfs, $\delta = (R_p/R_*)^2$, and n_{tr} is the number of transits. Values of σ_{cdpp} are reported for 14 different transit durations from 1.5 to 15 h for each Kepler star (Burke et al. 2015). The σ_{CDPP} value chosen for equation (5) is interpolated from the 14 reported CDPP values, to match the transit duration of the planet.

The number of transits for a planet is estimated by $n_{\text{tr}} = (T_{\text{baseline}} \times f_{\text{duty}})/P$, where P is the planet period, T_{baseline} is the total observing time for the Q1–Q16 catalogue (~ 1426 d) and f_{duty} is the duty cycle for the observed star; the fraction of valid observations over the observing baseline. Note that T_{baseline} and f_{duty} are reported for each star, accounting for systematics such as the differences in CCD detectors and pixels.

We define η_{detect} as the Kepler pipeline completeness, shown in Fig. 3. The pipeline completeness as a function of the MES is ap-

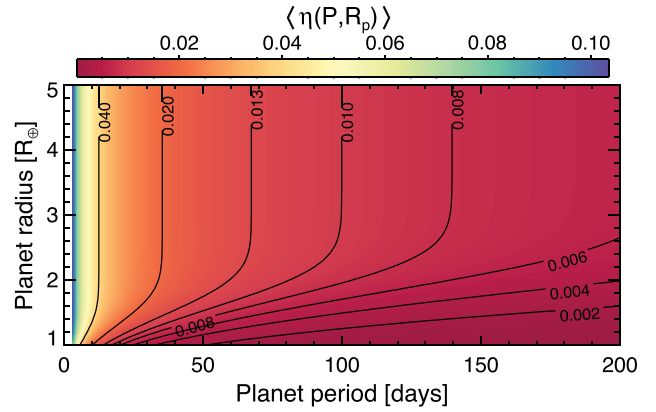


Figure 4. The probability of a planet transiting and being detected by the Kepler Q1–Q16 pipeline, $\langle \eta(P, R_p) \rangle$, over the planet period and planet radius parameter space of our simulations. The probability at each grid point is the average value across our stellar sample, the 63 128 stars that adhere to equation (2). For planets with radii exceeding $2.5 R_{\oplus}$, the pipeline detection efficiency $\eta_{\text{detect}} \approx 1$, and $\langle \eta(P, R_p) \rangle$ is well estimated by the transit probability η_{transit} .

proximately represented by the Γ cumulative distribution function:

$$\eta_{\text{detect}}(\text{MES}) = \frac{1}{c^b \Gamma(b)} \int_0^{\text{MES}-\beta} x^{b-1} e^{-x/c} dx, \quad (6)$$

where Γ is the Gamma function. For our sample of FGK dwarfs, $b = 4.35$, $c = 1.05$ and $\beta = 4.093$ (Christiansen et al. 2015).

To calculate the total probability of transit detection $\eta(P, R_p)$, we must also take into account the geometric transit probability η_{transit} of a planet,

$$\eta_{\text{transit}} = \frac{R_*}{a}, \quad (7)$$

where a is the semimajor axis of the planet. The product of these two equations gives the total transit detection probability $\eta(P, R_p)$, the probability of the planet transiting η_{transit} and the probability of the transiting planet being detected by the Kepler Q1–Q16 pipeline η_{detect} .

$$\eta(P, R_p) = \eta_{\text{transit}} \times \eta_{\text{detect}}. \quad (8)$$

Given an input star from our stellar sample (equation 2) and using equations (5)–(8), we can estimate the total transit and detection completeness of a simulated planet with planet parameters of period, radius and transit duration. Across our planetary parameter space used in this paper (equation 3), we estimate the mean total transit and detection completeness $\langle \eta(P, R_p) \rangle$, by taking the mean value of $\eta(P, R_p)$ at each grid point over all stars in our stellar sample. This is shown in Fig. 4, where $\langle \eta(P, R_p) \rangle$ ranges from ~ 0 to a maximum of ~ 0.1 . Transit and detection probabilities > 5 per cent only exist for planets with orbital periods $\lesssim 8$ d. It can be seen that the pipeline detection probability becomes important for planetary radii less than $2.5 R_{\oplus}$.

4 UNDERLYING PLANET DISTRIBUTIONS

Our simulated results of the number of stars with k detected transiting planets is reliant on an input planet radius and orbital period distribution, which has been one of the primary goals of the Kepler mission. The planet radius distribution is often modelled as a broken power law (Youdin 2011; Howard et al. 2012; Burke et al. 2015), with a logarithmic plateau at $\lesssim 2.5 R_{\oplus}$. This logarithmic plateau is

Table 1. Maximum likelihood PLDF parameters.

F_0	β_1	β_2	P_{brk}	α_1	α_2	R_{brk}
0.852	1.007	-0.932	15.332	-1.168	-4.906	2.740

also seen when the pipeline efficiency is probed using transit injection and recovery experiments (Petigura, Marcy & Howard 2013).

For orbital periods between 50 and 300 d, a single power law is sufficient to describe the orbital period distribution (Burke et al. 2015). Our parameter space includes planets with orbital periods less than 50 d, where the transit and detection completeness is more dynamic, particularly for periods $\lesssim 15$ d (Fig. 4). For this parameter space, a single power law is not sufficient, and we model the orbital period distribution as a broken power law.

The planet radius and orbital period distributions are combined into a planet distribution function (PLDF), in this case composed of a broken power law for the distribution of orbital periods, and a broken power law for the distribution of planetary radii.

Our PLDF has seven parameters, F_0 , β_1 , β_2 , P_{brk} , α_1 , α_2 , R_{brk} , where F_0 is the number of planets per star within our parameter space, and R_{brk} and P_{brk} are the transition points between the two power laws for the planet radius and orbital period, respectively,

$$\frac{df}{dP dR_p} = C F_0 g(P, R_p)$$

$$= \begin{cases} C F_0 P^{\beta_1} R_p^{\alpha_1} & \text{if } P < P_{\text{brk}} \text{ and } R_p < R_{\text{brk}} \\ C F_0 P^{\beta_1} R_p^{\alpha_2} R_{\text{brk}}^{\alpha_1 - \alpha_2} & \text{if } P < P_{\text{brk}} \text{ and } R_p \geq R_{\text{brk}} \\ C F_0 P^{\beta_2} P_{\text{brk}}^{\beta_1 - \beta_2} R_p^{\alpha_1} & \text{if } P \geq P_{\text{brk}} \text{ and } R_p < R_{\text{brk}} \\ C F_0 P^{\beta_2} P_{\text{brk}}^{\beta_1 - \beta_2} R_p^{\alpha_2} R_{\text{brk}}^{\alpha_1 - \alpha_2} & \text{if } P \geq P_{\text{brk}} \text{ and } R_p \geq R_{\text{brk}}, \end{cases} \quad (9)$$

where the power-law exponents α_1 , α_2 and β_1 , β_2 represent the exponents for the orbital period and the planet radius distribution respectively, either side of the power-law breaks (See Table 1).

For each set of model parameters in an underlying PLDF, an expected number of planet detections is computed by convolving the PLDF with $\langle \eta(P, R_p) \rangle$ (Fig. 4). The number of expected detections for an underlying PLDF is then compared to the number of Kepler Q1–Q16 detections by maximizing the Poisson likelihood of the PLDF. The maximum likelihood derivation for our PLDF (equation 9) is shown in Appendix B, with maximum likelihood parameters of indicating breaks in the power-law distributions at ~ 15 d and $\sim 2.7 R_{\oplus}$ for orbital periods and planetary radii, respectively. The break in the orbital period distribution corresponds to a peak in the distribution, whereas the break in the planet radius distribution corresponds to the logarithmic planet plateau for $R_p \lesssim 2.7 R_{\oplus}$. These results appear to be consistent with Foreman-Mackey, Hogg & Morton (2014), where breaks in the logarithmic orbital period and planet radius rates are indicated at ~ 20 d and ~ 2 – 3 Earth radii, respectively.

We can marginalize our maximum likelihood PLDF in terms of orbital period and planet radius. This is shown in Figs 5 and 6, respectively, where the thick red lines represent our marginalized maximum likelihood PLDF, which is the estimated underlying planet distribution. The dashed red lines indicate the corresponding transit detected distribution, after applying the mean total transit and detection probability $\langle \eta(P, R_p) \rangle$ for the stars in our sample.

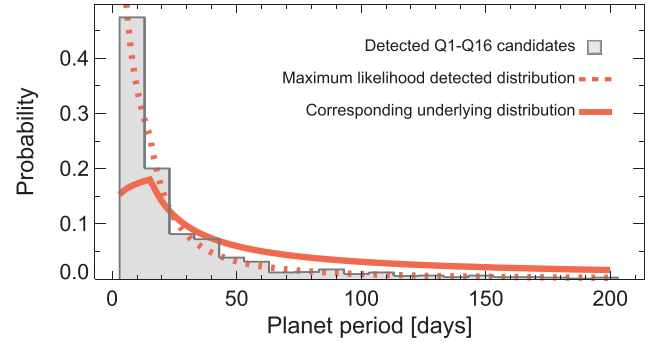


Figure 5. The estimated underlying period distribution used for populating simulated planetary systems in this paper. The underlying distribution is the marginalized orbital period PLDF maximum likelihood model (equation 9 and Table 1). The expected detected distribution (dashed red line), results when the underlying distribution is convolved with the average total transit and detection probability $\langle \eta(P, R_p) \rangle$ for the stars in our sample. This can be compared with the detected Q1–Q16 Kepler candidates (grey histogram).

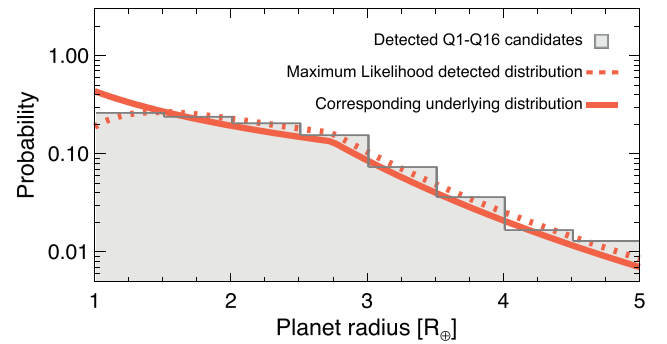


Figure 6. The same as Fig. 5, except for the planet radius distribution. The estimated underlying distribution is given by a broken power law with a break at ~ 2.7 Earth radii (Table 1).

When producing model planetary systems in Section 5, we assign orbital periods and planetary radii by drawing randomly from the maximum likelihood underlying distributions, shown in Figs 5 and 6.

4.1 Parametrizing planet multiplicity

For a set of model planetary systems, we need to assume a distribution for the inherent number of planets per star within our parameter space, N_{pl} . In this paper, we trial two different N_{pl} distributions.

The first trial distribution is a modified Poisson distribution $N_{\text{pl, Poi}}$ (Fang & Margot 2012). Each star is assigned a random number of planets, drawn from a Poisson distribution with mean μ . Stars drawn with zero planets are redrawn from the same Poisson distribution, until all 10^6 model planetary systems are populated with planets, resulting in a final mean $\geq \mu$.

The second trial distribution is a modified exponential distribution $N_{\text{pl, exp}}$ (Gaidos, Mann, Kraus & Ireland 2016) and is produced in the same way as $N_{\text{pl, Poi}}$, except that stars are assigned a number of planets drawn from an exponential distribution with mean μ . The mode of the exponential distribution is always 0, resulting in a natural tendency for more planetary systems to contain a single transiting planet rather than multiple transiting planets. It has been shown that when an exponential distribution is used to model the inherent number of planets per star, no Kepler dichotomy is

required (Gaidos et al. 2016). We include this trial distribution for comparative purposes.

5 PRODUCING MODEL PLANETARY SYSTEMS

In our simulations, we assume two different planetary disc models, and two different distributions for the number of planets per star N_{pl} , resulting in simulations with four unique combinations of model assumptions. For a given set of model assumptions, we generate populations of planetary systems across a grid. The mean of the number of planets per star μ ranges from 0.5 to 3.5 in steps of 0.1. For the flared disc model, the mode of the Rayleigh distributed mutual inclinations ranges from 0° to 5° in steps of 0.1° . Similarly for the flat disc model, the standard deviation of the height above the invariable plane ranges from 0 to $5 R_*$ in steps of $0.1 R_*$.

This results in a total of 1500 grid points for each set of model assumptions, with 10^6 model planetary systems generated at each grid point. Each model planetary system is produced as follows:

1. A random star is chosen from our sample of 63 128 Kepler stars outlined in Section 2, and its mass and radius are assigned to the star in the model system.
2. The angle to the system's invariable plane relative to the observer (θ) (Fig. A1), is chosen from a random point on a sphere: $0 \leq \cos[(\theta)] \leq 1$.
3. The number of planets in the system n_i is drawn randomly, according to the assumed N_{pl} distribution from Section 4.1, with a mean value based on the current grid point.
4. The radii of the n_i planets are drawn from the underlying distribution in Section 4 ($1 R_\oplus < R_p < 5 R_\oplus$), and converted to their corresponding masses.⁴
5. The periods of the n_i planets are drawn randomly from the underlying distribution in Section 4 ($3 \text{ d} < P < 200 \text{ d}$), and converted to their corresponding semimajor axes, using the stellar properties of the assigned Kepler star.
6. The dynamical stability of the system is estimated by testing the stability of sets of three sequential planets, or pairwise if $n_i = 2$. If any set of planets in the system is deemed unstable, the system is labelled unstable and new planet periods for all n_i planets are redrawn as in step 5. See Section C1 for a complete description of estimating the stability of a system, including termination criteria.
7. The inclinations of the planetary orbital planes relative to the observer, are determined from $\langle \theta \rangle$ (step 2) and the assumed planetary disc model (Section 1.4), and the parameter value at the current grid point. See Appendix C2 for a complete description of how planet inclinations are assigned for flat and flared disc models.

The above steps generate the 10^6 model systems according to the assumed disc model, the assumed planet multiplicity distribution, the current grid point parameters and the underlying planet period and radius distributions. The final step is to estimate which simulated planets would be detected by the Kepler Q1–Q16 pipeline, and compare this detected sample to the observed Q1–Q16 detections.

5.1 Determining transiting and detected planets

Once planetary inclinations are assigned, the model system is complete and we test for transiting planets. We define a transiting planet by its impact parameter b , where a planet is defined to transit if:

$$b = \frac{a}{R_*} \cos i \leq 1, \quad (10)$$

⁴ $M_p \approx (R_p/a)^b$, where $a \sim 1.11$ and $b \sim 2.41$.

where R_* , a and i were determined from steps 1, 5 and 7, respectively.

For each simulated transiting planet, we estimate the MES (equation 5). The MES is dependent on stellar properties, along with the planet's orbital period, radius and transit duration. Circular orbits are assumed when estimating transit durations. The planet's MES is then used to estimate the pipeline detection efficiency η_{detect} (equation 6). For each simulated transiting planet, a uniform random number Y_m is drawn between 0 and 1. A simulated planet is labelled as detected if it transits, and if its pipeline detection efficiency $\eta_{\text{detect}} > Y_m$. All simulated planets that meet this criteria are added to the detected planet sample for the grid point, X_{ij} , where i and j represent the current grid point.

6 COMPARING SIMULATED AND OBSERVED PLANET DETECTIONS

The simulations outlined in Section 5 were performed across a grid for the four sets of model assumptions. For each grid point, the simulated planet detections X_{ij} are used to generate two distributions, the system multiplicity vector $\hat{N}_{k,ij}$ (equation 1) and the distribution of orbit normalized transit duration ratios ξ_{ij} (Steffen et al. 2010). Unlike the $\hat{N}_{k,ij}$ distribution, the ξ_{ij} distribution only consists of model systems with two or more detected transiting planets. For a pair of planets orbiting the same star,

$$\xi = \frac{T_{\text{dur,in}}/P_{\text{in}}^{1/3}}{T_{\text{dur,out}}/P_{\text{out}}^{1/3}}, \quad (11)$$

where T_{dur} and P are the transit durations and the periods for the inner and outer planets, given by the subscripts in and out, respectively. For each unique planet pair in a system, ξ is calculated, giving $n_i(n_i + 1)/2$ values of ξ for a star with n_i planets. For each grid point we generate the ensemble ξ_{ij} distribution by calculating the ξ value for each unique pair of simulated transit detections orbiting the same star, across all 10^6 model systems. For a deeper discussion of ξ , see Appendix D.

The $\hat{N}_{k,ij}$ and ξ_{ij} distributions are compared to the \hat{N}_k and ξ distributions of the Kepler Q1–Q16 candidates, and are used to assess the goodness of fit at each grid point. We perform a χ^2 goodness of fit test (equation 12) comparing the simulated $\hat{N}_{k,ij}$ to the observed \hat{N}_k for our parameter space (equation 4). We scale $\hat{N}_{k,ij}$ such that $\sum \hat{N}_{k,ij} = \sum \hat{N}_k$. To compensate for the poor quality of the χ^2 test with low cell counts, values less than 5 are merged into their adjacent cells.

$$\chi^2 = \sum_{k=1}^n \frac{(\hat{N}_k - \hat{N}_{k,ij})^2}{\hat{N}_{k,ij}}. \quad (12)$$

Similarly, we perform a two-sample Kolmogorov–Smirnov (KS) test between the simulated ξ_{ij} distribution at each grid point and the ξ distribution of the observed Q1–Q16 Kepler candidates within our parameter space.

6.1 Flared disc and Poisson distributed planets per star

In the top panel of Fig. 7, $\hat{N}_{k,ij}$ is compared to \hat{N}_k at each grid point, under the assumption of a flared planetary disc and a Poisson distributed number of planets per star. The χ^2 values are represented by the 1σ , 2σ and 3σ values relative to the best fit. As expected, no good fit is found to the \hat{N}_k distribution, as is the case in the majority of previous studies (Lissauer et al. 2011; Johansen et al. 2012; Ballard & Johnson 2016; Gaidos et al. 2016).

The bottom panel displays the resulting p values from the KS test between the ξ_{ij} and ξ distributions. The orbital normalized transit duration ratios favour mutual inclinations with a mode between 1.5°

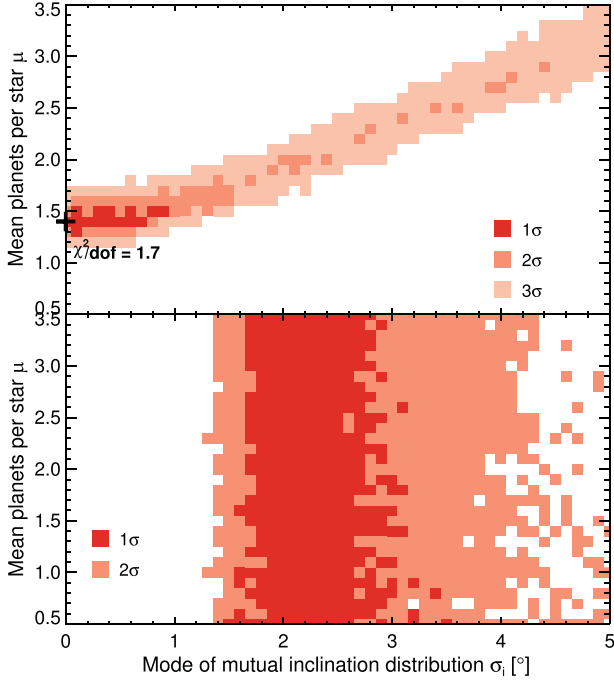


Figure 7. Comparing the simulated planet detections to the observed Q1–Q16 Kepler candidates, for Poisson distributed number of planets per star N_{pl} with mean μ , and a flared disc model (Rayleigh distributed mutual inclinations with mode σ_i). Top: comparing the Kepler Q1–Q16 \hat{N}_k distribution (equation 4) to the simulated $\hat{N}_{k,ij}$ distribution for each grid point. Highly coplanar systems are favoured. Bottom: comparing the Kepler Q1–Q16 ξ distribution (equation 11) to the simulated ξ_{ij} distribution for each grid point. Contrary to comparing \hat{N}_k distributions, coplanar systems with $\sigma_i \lesssim 1.3^\circ$ are ruled out.

and 4° , consistent with all previous studies shown in Appendix E. The mean number of planet per star cannot be determined from the ξ_{ij} distribution alone.

It is clear from Fig. 7 that the best-fitting regions (dark red) of the two tests do not appear consistent. Comparing multiplicity vectors favours near-coplanar mutual inclinations, with a mode $\lesssim 1^\circ$ (top panel). However, modes $\lesssim 1.5^\circ$ are ruled out by comparing orbit normalized transit duration ratios (bottom panel).

6.2 Flat disc and Poisson distributed planets per star

For the set of simulations with a Poisson distributed N_{pl} and a flat disc model, the two tests appear more consistent (Fig. 8). Unlike for the flared disc model, the best-fitting $\hat{N}_{k,ij}$ is a good match to \hat{N}_k , giving a χ^2/dof of 0.9, indicating that no Kepler dichotomy is required.

While Gaussian disk thicknesses $> 2R_*$ are supported by comparing multiplicity vectors, comparing orbit normalized transit durations refines the disk thickness to $1R_* \lesssim Z_0 \lesssim 2R_*$. There is significant overlap between the two tests within this region.

6.3 Combining independent tests

The results from comparing the \hat{N}_k and ξ distributions can be combined in order to estimate the overall best-fitting parameters, for a given set of model assumptions. The p values from each test are combined using Fisher’s method into a single test statistic,

$$\chi_{\text{combined}}^2 \approx -2 \sum_{m=1}^M \ln p_m, \quad (13)$$

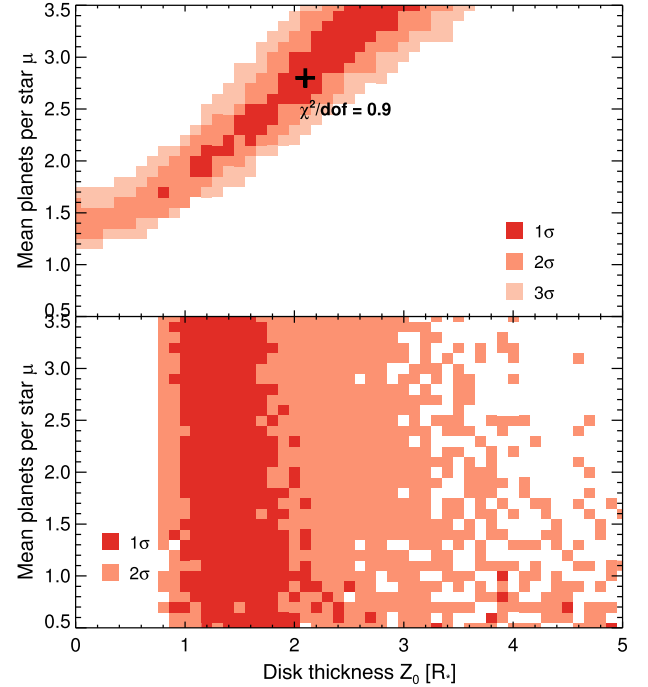


Figure 8. The same as Fig. 7, except for a flat disc model instead of a flared disc model. Both simulated \hat{N}_k and ξ distributions are consistent with the detected Kepler Q1–Q16 candidates for a flat disc model with Gaussian disc thicknesses between ~ 1 and ~ 3 stellar radii.

where M is the number of tests combined and p_m is the p value of the m th test. The degrees of freedom is given by $2M$, where in this case $M = 2$. We use this combined statistic to produce a probability grid, P_{combined} , across the parameter space for each set of model assumptions. P_{combined} is derived from the likelihood $P_{ij} \propto \exp(-\chi_{\text{combined},ij}^2/2)$ and the requirement $\sum P_{ij} = 1$.

Fig. 9 displays the probability grids for each set of model assumptions, along with the best-fitting point and the 1σ and 2σ probability contours. Panel (a) of Fig. 9 combines the tests of Fig. 7 and panel (b) combines the tests of Fig. 8. A similar process is involved for panels (c) and (d), where the number of planets per star N_{pl} is drawn from an exponential distribution. The intermediate figures for these two panels are not displayed for succinctness.

7 RESULTS AND DISCUSSION

7.1 Flared disc model

Our result for a flared disc with a Poisson distributed number of planets per star, appears to be compatible with the majority of previous analyses. We find a mean number of planets per star $\mu = 2.0_{-0.2}^{+0.3}$, over our parameter space, [$3 \text{ d} < P < 200 \text{ d}$] and [$1 R_\oplus < R_p < 5 R_\oplus$]. For a similar orbital period and planet radius parameter space, Gaidos et al. (2016) find $\mu = 2.2 \pm 0.3$ for Kepler M dwarfs. Fang & Margot (2012) report $\mu \sim 1.5$ for $R_p > 1.5 R_\oplus$, where the reduction in μ likely comes from the exclusion of planets with radii between $1.0 R_\oplus < R_p < 1.5 R_\oplus$.

Similarly, we find the mode of the Rayleigh distributed mutual inclinations is given by $\sigma_i = 2.3_{-0.4}^{+0.9}$ deg, consistent with the bulk of previous results with $\sigma_i \sim 2^\circ$ (Lissauer et al. 2011; Fang & Margot 2012; Figueira et al. 2012; Johansen et al. 2012; Tremaine & Dong 2012; Fabrycky et al. 2014; Ballard & Johnson 2016; Gaidos et al. 2016).

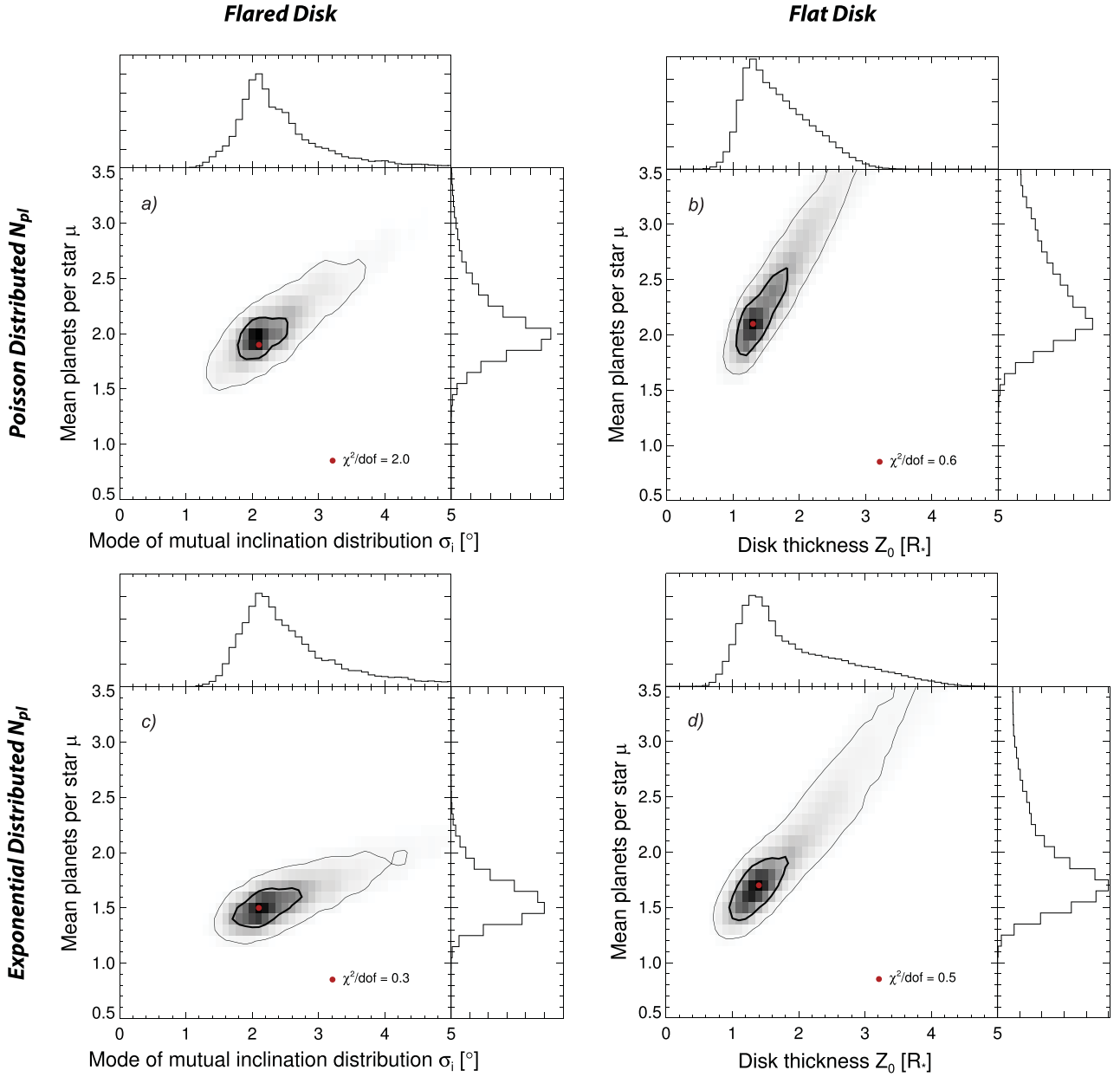


Figure 9. The combined probability distributions P_{combined} for our four sets of model assumptions. P_{combined} takes into account the goodness of fit between the simulated $\hat{N}_{k,ij}$ distributions and the Kepler Q1–Q16 \hat{N}_k , and the consistency of the simulated $\hat{\xi}_{ij}$ distributions and Q1–Q16 ξ distribution. For example, panel (a) corresponds to the combined top and bottom panels of Fig. 7. Each panel represents a different set of model assumptions, specifically, a flared disc and Poisson distributed N_{pl} (panel a), a flat disc and Poisson distributed N_{pl} (panel b), a flared disc and exponential distributed N_{pl} (panel c), a flat disc and exponential distributed N_{pl} (panel d). The combined best-fitting grid point is shown as a filled red circle for each set of simulations, along with the 1σ and 2σ probability contours. The only set of model systems which does not match the Q1–Q16 Kepler observations well, is when the number of planets per star N_{pl} is Poisson distributed with a flared planetary disc. Only this combination of model assumptions requires a dichotomous planetary system population, i.e. the Kepler dichotomy.

We are unable to achieve a good match to the Kepler Q1–Q16 detections for a flared disc model, contrary to the reported result by Fang & Margot (2012), where a flared disc model reproduced the \hat{N}_k distribution without the need for a Kepler dichotomy. The discrepancy likely comes from the unique N_{pl} distribution chosen by Fang & Margot (2012), a ‘bounded uniform’ distribution. The bounded uniform distribution is produced by first choosing a maximum number of planets $n_{i,\text{max}}$ from a Poisson distribution, then choosing the number of planets in the system n_i from a uniform distribution between 1 and $n_{i,\text{max}}$.

It has previously been shown that the Kepler \hat{N}_k distribution can be matched without the need for a Kepler dichotomy, when N_{pl} is drawn from an exponential distribution (Gaidos et al. 2016). We find that the Kepler sample is consistent with $\sigma_i = 2.4^{+0.9}_{-0.5}$ deg and $\mu = 1.6^{+0.3}_{-0.2}$ drawn from an exponential distribution. Here, we disagree with Gaidos et al. (2016), who preferred near-coplanar mutual inclinations. While we also achieve good fits for near-coplanar orbital planes, comparing ξ distributions strongly rules out mutual inclinations $\lesssim 1.4^\circ$. This illustrates the importance of modelling both \hat{N}_k and ξ

distributions, where Gaidos et al. (2016) only modelled the \hat{N}_k distribution.

7.2 Flat disc model

For a flat planetary disc model (Dullemond & Monnier 2010), a good fit to the Kepler candidates can be achieved when the number of planets per star is drawn from both a Poisson or exponential distribution. That is, independent of the N_{pl} distribution chosen, the flat disc model removes the need for a Kepler dichotomy. When N_{pl} is drawn from a Poisson distribution, we find $Z_0 = 1.6_{-0.4}^{+0.6} R_*$ and $\mu = 2.4_{-0.4}^{+0.6}$. Notably, the mean number of planets per star μ is consistent between the assumed planetary disc models.

We use a flat planetary disc model with a Gaussian disc thickness Z_0 . We can compare this value to the inner Solar system (Fig. 2). For the inner Solar system planets, $Z_{\text{max}} \approx 8 R_*$, giving $Z_0 \approx 5 R_*$, where $Z_0 \approx 2 Z_{\text{max}}/\pi$. This is significantly larger than our derived value of $Z_0 = 1.6_{-0.4}^{+0.6} R_*$ for our sample of closely packed Kepler systems. This may give some indication of the flat disc model's applicability at larger semimajor axes, or may be reflective of the different parameter spaces probed.

8 SUMMARY AND CONCLUSION

We estimate the inherent orbital period and planet radius distributions for the Kepler Q1–Q16 catalogue, within the parameter space [$3 \text{ d} < P < 200 \text{ d}$] and [$1 R_{\oplus} < R_p < 5 R_{\oplus}$]. We find that both distributions are well described by broken power laws, with breaks occurring at $\sim 15 \text{ d}$ and $\sim 2.7 R_{\oplus}$. These inherent distributions are used to populate model planetary systems for flat and flared planetary disc models, and for the number of planets per star N_{pl} drawn from Poisson and exponential distributions.

We confirm that a flared planetary disc model with N_{pl} drawn from a Poisson distribution is not consistent with the Kepler detections. We also confirm that Kepler detections are well matched when N_{pl} is drawn from an exponential distribution, without the need to invoke a dichotomous planetary system population. In this paper, we use a flat inner planetary disc model, where planets with smaller periods tend to have larger inclinations. When a flat rather than a flared planetary disc model is assumed, model systems are consistent with Kepler detections, without the requirement of a Kepler dichotomy and independent of the chosen N_{pl} distribution.

We find that the mean number of planets per star μ is largely model independent, ~ 2.0 when N_{pl} is drawn from a Poisson distribution, and ~ 1.6 when N_{pl} is drawn from an exponential distribution, for [$3 \text{ d} < P < 200 \text{ d}$] and [$1 R_{\oplus} < R_p < 5 R_{\oplus}$]. This contrasts with the Solar system where there are 0 planets within this parameter space.

Similarly, we find for a flared planetary disc model, mutual inclinations are distributed with a mode $\sim 2.2^\circ$. For a flat planetary disc model, the Gaussian disc thickness $Z_0 \sim 1.5 R_*$, much lower than the $\sim 5 R_*$ of the inner Solar system.

8.1 The Kepler dichotomy

The underproduction of model systems with a single detected transiting planet has been well studied. This has led to the invocation of a dichotomous planetary system population, where one population suppresses the number of detected transiting planets, resulting in a higher likelihood of producing a single detected transiting planet. Many physical explanations for the existence of the dichotomy have been put forward (Johansen et al. 2012; Weissbein, Steinberg

& Sari 2012; Hansen & Murray 2013; Moriarty & Ballard 2016; Spalding & Batygin 2016; Lai & Pu 2017).

Dawson, Lee & Chiang (2016) generated sets of planetary systems with various gas depletion factors using N -body simulations of planetary embryos. No set of simulations was a good match to the period ratio, Δ (equation C2), planet multiplicity and ξ distributions of the observed Kepler sample. Some improvement was found when simulated planetary systems were allowed to be a mix of ‘dynamically hot’ and ‘dynamically cold systems’. However, this improvement becomes less pronounced when taking into account the partial correlations between these distributions, particularly between ξ and Δ .

It has also been shown that the requirement of the dichotomy is not robust to the assumed distribution for the number of planets per star (Fang & Margot 2012; Gaidos et al. 2016). This is confirmed in this paper, and in addition, we show that a planetary system dichotomy is also not required for a flat inner planetary disc model. This result is independent of the choice of distribution for the number of planets per star N_p . We emphasize that we apply the flat planetary disc model only to the short period range of Kepler candidates.

Of the sets of model assumptions explored in this paper, the need for a Kepler dichotomy only exists for a flared inner planetary disc, with the number of planets per star drawn from a Poisson distribution.

The Kepler dichotomy describes the apparent need for a dichotomous planetary system population, with respect to a star's probability of producing multiple transiting planets. We show that the Kepler dichotomy is only required under specific model assumptions. Specifically, when the inner part of a planetary disc is assumed to be flared, while also requiring the number of planets per star to be Poisson distributed. When removing either or both of these assumptions, the need for a Kepler dichotomy disappears.

REFERENCES

- Ballard S., Johnson J. A., 2016, *ApJ*, 816, 66
 Burke C. J. et al., 2015, *ApJ*, 809, 8
 Chambers J. E., Wetherill G. W., Boss A. P., 1996, *Icarus*, 119, 261
 Christiansen J. L. et al., 2012, *PASP*, 124, 1279
 Christiansen J. L. et al., 2015, *ApJ*, 810, 95
 Dawson R. I., Lee J., Chiang E., 2016, *ApJ*, 822, 54
 Dullemond C. P., Monnier J. D., 2010, *AR&A*, 48, 205
 Fabrycky D. C. et al., 2014, *ApJ*, 790, 146
 Fang J., Margot J.-L., 2012, *ApJ*, 761, 92
 Figueira P. et al., 2012, *A&A*, 541, A139
 Foreman-Mackey D., Hogg D. W., Morton T. D., 2014, *ApJ*, 795, 64
 Gaidos E., Mann A. W., Kraus A. L., Ireland M. J., 2016, *MNRAS*, 457, 2877
 Gladman B., 1993, *Icarus*, 106, 247
 Hadden S., Lithwick Y., 2014, *ApJ*, 787, 80
 Hansen B. M. S., Murray N., 2013, *ApJ*, 775, 53
 Howard A. W. et al., 2012, *ApJS*, 201, 15
 Johansen A., Davies M. B., Church R. P., Holmelin V., 2012, *ApJ*, 758, 39
 Lai D., Pu B., 2017, *AJ*, 153, 42
 Lissauer J. J. et al., 2011, *ApJS*, 197, 8
 Moorhead A. V. et al., 2011, *ApJS*, 197, 1
 Moriarty J., Ballard S., 2016, *ApJ*, 832, 34
 Mullally F. et al., 2015, *ApJS*, 217, 31
 Petigura E. A., Marcy G. W., Howard A., 2013, *ApJ*, 770, 69
 Spalding C., Batygin K., 2016, *ApJ*, 830, 5
 Steffen J. H. et al., 2010, *ApJ*, 725, 1226
 Tremaine S., Dong S., 2012, *AJ*, 143, 94
 Weissbein A., Steinberg E., Sari R., 2012, *ApJ*, preprint (arXiv:1203.6072)
 Youdin A. N., 2011, *ApJ*, 742, 38

APPENDIX A: INCLINATION ANGLES OF PLANETARY ORBITAL PLANETS

There are a number of different angles used in the literature that have all been referred to as the planet inclination. Where we have used an inclination angle, we have attempted to be as explicit as possible. The below figure illustrates different inclination angles used throughout the paper.

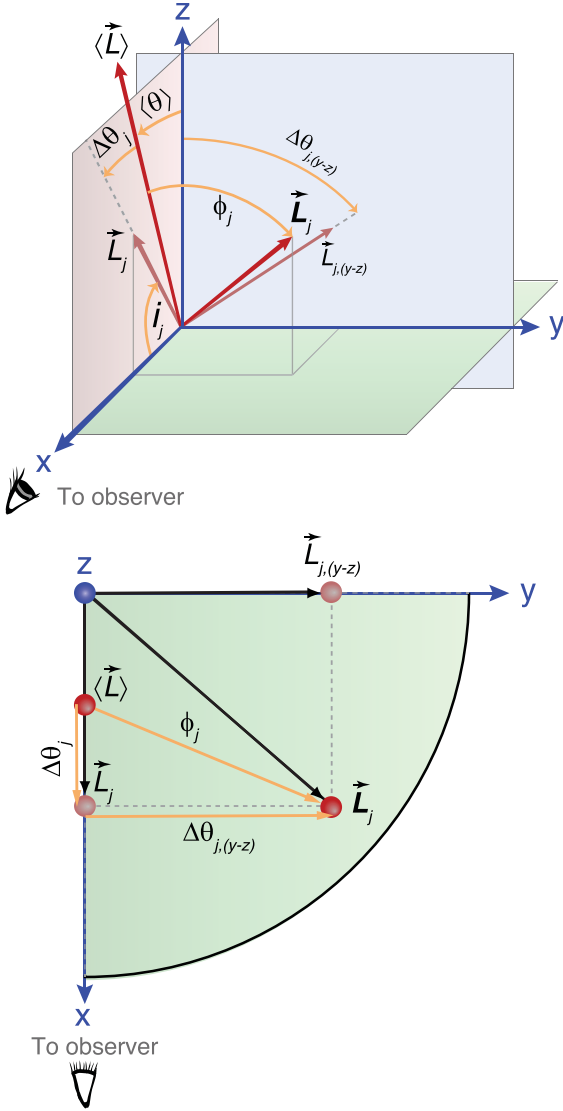


Figure A1. Top: the inclination angles used in this paper, with the observer in the direction of the x -axis. We have chosen our coordinate system (without the loss of generality) such that the invariable plane vector $\langle \vec{L} \rangle$ is in the x - z plane. The angular momentum vector of the planet is \vec{L}_j and the projection of \vec{L}_j on to the x - z plane is given by $\vec{L}_{j,(y-z)}$. The j subscript refers to an individual planet. The projected inclination of the j th planet's orbital plane relative to the observer is represented by i_j , typically reported by transit and radial velocity detections (e.g. $M \sin i_j$). The coplanarity of planets refers to the distribution of ϕ_j , the angle between the invariable plane of the system and the orbital planes of the planets. The component of ϕ_j that the observer can probe is $\Delta\theta_j$ (whose distribution is plotted in the lower panels of Fig. 1), while $\Delta\theta_{j,(y-z)}$ is the orthogonal component of the inclination that typically cannot be measured by the observer. Bottom: the coordinate system from the top panel viewed from above and compressed to two dimensions (the z -axis points out of the page). The filled circles represent the tops of the vectors from the top panel.

APPENDIX B: PLANET DISTRIBUTION FUNCTION

Our PLDF has seven free parameters, $F_0, \beta_1, \beta_2, P_{\text{brk}}, \alpha_1, \alpha_2, R_{\text{brk}}$.

$$\frac{df}{dP dR_p} = C F_0 g(P, R_p) = \begin{cases} C F_0 P^{\beta_1} R_p^{\alpha_1} & \text{if } P < P_{\text{brk}} \text{ and } R_p < R_{\text{brk}} \\ C F_0 P^{\beta_1} R_p^{\alpha_2} R_{\text{brk}}^{\alpha_1 - \alpha_2} & \text{if } P < P_{\text{brk}} \text{ and } R_p \geq R_{\text{brk}} \\ C F_0 P^{\beta_2} P_{\text{brk}}^{\beta_1 - \beta_2} R_p^{\alpha_1} & \text{if } P \geq P_{\text{brk}} \text{ and } R_p < R_{\text{brk}} \\ C F_0 P^{\beta_2} P_{\text{brk}}^{\beta_1 - \beta_2} R_p^{\alpha_2} R_{\text{brk}}^{\alpha_1 - \alpha_2} & \text{if } P \geq P_{\text{brk}} \text{ and } R_p \geq R_{\text{brk}}, \end{cases} \quad (\text{B1})$$

where F_0 is the number of planets per star within our parameter space, R_{brk} and P_{brk} are the transition points between the two power laws for the planet radius and orbital period, respectively. The normalization constant C is calculated from the requirement:

$$\int_{R_{\text{min}}}^{R_{\text{max}}} \int_{P_{\text{min}}}^{P_{\text{max}}} C g(P, R_p) dP dR_p = 1, \quad (\text{B2})$$

where the integration limits $R_{\text{min}}, R_{\text{max}}, P_{\text{min}}$ and P_{max} are given in equation (3).

We follow Youdin (2011) and Burke et al. (2015) by implementing a Poisson likelihood for our PLDF. By maximizing this likelihood, we can obtain best-fitting parameters for our model.

$$\ln(L) \propto \left[\sum_{i=1}^{N_{\text{pl}}} \ln(C F_0 g(P, R_p)) \right] - N_{\text{exp}}, \quad (\text{B3})$$

where N_{exp} is the expected number of planet detections for the set of model parameters, and is given by

$$N_{\text{exp}} = C F_0 \int_{R_{\text{min}}}^{R_{\text{max}}} \int_{P_{\text{min}}}^{P_{\text{max}}} \left[\sum_{j=1}^{N_*} \eta_j(P, R_p) \right] g(P, R_p) dP dR_p, \quad (\text{B4})$$

where $\eta_j(P, R_p) = \eta_{\text{detect}} \times \eta_{\text{transit}}$ is the combined transit and pipeline detection efficiency of the j th star for the specified period and radius. The pipeline detection efficiency η_{detect} is given by equation (6) and the transit probability $\eta_{\text{transit}} = R_*/a$, where a is the semimajor axis.

We calculate $[\sum_{j=1}^{N_*} \eta_j(P, R_p)]$ for a grid in orbital period and planet radii, in bins of 1.5 d and 0.05 R_{\oplus} , respectively. For each grid point, we sum over all stars in our sample. The mean combined transit and pipeline detection efficiency $\langle \eta(P, R_p) \rangle$ can then be found by dividing this term by the number of stars in our sample, N_* .

APPENDIX C: SIMULATED PLANETARY SYSTEMS

C1 Testing the stability of sequential planet pairs

The dynamical spacing Δ describes the separation of two planets in units of their mutual Hill's radius. The mutual Hill's radius of two planets is given by

$$R_{\text{H},ij} = \left(\frac{m_i + m_j}{3M_*} \right)^{1/3} \frac{a_i + a_j}{2}, \quad (\text{C1})$$

where m_i and m_j are the planet masses for the inner and outer planets, respectively. The dynamical spacing Δ is the semimajor axis spacing of the two planets, in units of the mutual Hill's radius.

$$\Delta_{ij} = \frac{a_j - a_i}{R_{H,ij}}, \quad (\text{C2})$$

where a_i and a_j are the semimajor axes of the inner and outer planets, respectively. Analytic stability solutions exist for a system that contains exactly two planets, $\Delta_{ij} \gtrsim 3.46$ (Gladman 1993; Chambers, Wetherill & Boss 1996), although it is not possible to ensure this requirement for our simulated systems⁵. For systems with $n_i \geq 3$, we use an empirical stability criteria for two adjacent planet pairs (three sequential planets). A set of three sequential planets with indices i, j and k is deemed unstable when

$$\Delta_{ij} + \Delta_{jk} < 18, \quad (\text{C3})$$

where Δ_{ij} and Δ_{jk} are the dynamical spacing of the inner and outer planet pair from the three sequential planets (Lissauer et al. 2011). If there are only two simulated planets in a system, $\Delta_{ij} < 10$ results in the system being labelled unstable.

Should any set of planets fail the above stability criteria, the system is deemed unstable and new planet periods are redrawn for all n_i planets as in step 5. New planetary radii are not redrawn, since passing the stability criteria is biased towards sets of planets with small planetary radii, where stability is more easily achieved. Redrawing planetary radii immediately would result in a simulated R_p distribution skewed towards small R_p , relative to the underlying distribution in Section 4. Should the stability criteria fail 10^3 times for the same set of planetary radii, new R_p and periods for all n_i planets are redrawn as in step 4.

C2 Orbital plane inclinations relative to the observer

Once stability has been established for a model system, each planet is then assigned an inclination relative to the observer, the i variable commonly seen in transit and radial velocity detections.

For Rayleigh distributed mutual inclinations (flared disc in Fig. 1), i is assigned as follows. An inclination ϕ is drawn from a Rayleigh distribution with mode $\sigma_\phi/\sqrt{2}$, where σ_ϕ is the mode of the Rayleigh distributed mutual inclinations. The factor of $1/\sqrt{2}$ is a conversion factor between the Rayleigh distributed mutual inclinations and the Rayleigh distributed planet inclinations around the invariable plane. The orbital plane of the planet is then rotated by a random uniform angle Ω , giving

$$i_{\text{flare}} = \langle \theta \rangle + \phi \cos(\Omega). \quad (\text{C4})$$

For a flat disc (Fig. 1), the perpendicular height above the invariable plane Z_0 is drawn from a Gaussian distribution with a mean of 0 and standard deviation σ_Z , in units of stellar radii. For a flat disc, unlike a flared disc, the assigned inclination i is dependent on the semimajor axis of the planet. Again, the orbital plane of the planet is rotated by a random uniform angle Ω , to account for a random

viewing angle.

$$i_{\text{flat}} = \langle \theta \rangle + \arcsin(Z_0/a) \cos(\Omega) \quad (\text{C5})$$

resulting in a tendency for larger inclinations for close-in planets and vice versa (right-hand panel of Fig. 1).

APPENDIX D: ORBIT-NORMALIZED TRANSIT DURATION RATIO ξ

For a planet that transits through the centre of its star:

$$2R_* \approx v_{\text{orb}} T_{\text{dur}}, \quad (\text{D1})$$

where v_{orb} and T_{dur} represent the orbital velocity (assuming a circular orbit) and the transit duration of the planet, respectively. Note that for the Kepler sample, the simplification of a circular orbit is justified since ξ is weakly dependent on eccentricity (Fabrycky et al. 2014). In addition, eccentricity values for the Kepler sample are generally found to be associated with near-circular orbits (e.g. Fabrycky et al. 2014; Hadden & Lithwick 2014; Dawson et al. 2016), or with mean values around ~ 0.1 (Moorhead et al. 2011; Hansen & Murray 2013).

When the transit is not through the centre of the star ($2R_* = 2\sqrt{R_*^2 - b^2}$):

$$2\sqrt{R_*^2 - b^2} = v_{\text{orb}} T_{\text{dur}}, \quad (\text{D2})$$

where b is the impact parameter representing the transiting planet. For a pair of planets that transit the same host star:

$$2\sqrt{R_*^2 - b_{\text{in}}^2} = T_{\text{dur,in}} v_{\text{orb,in}}, \quad (\text{D3})$$

$$2\sqrt{R_*^2 - b_{\text{out}}^2} = T_{\text{dur,out}} v_{\text{orb,out}}, \quad (\text{D4})$$

where the 'in' and 'out' subscripts represent the inner and outer planets, respectively. From Kepler's 3rd law:

$$v_{\text{orb,in}} \propto \frac{a_{\text{in}}}{P_{\text{in}}} \propto P_{\text{in}}^{-1/3}.$$

Dividing D3 by D4:

$$\frac{\sqrt{R_*^2 - b_{\text{in}}^2}}{\sqrt{R_*^2 - b_{\text{out}}^2}} = \frac{T_{\text{dur,in}}/P_{\text{in}}^{1/3}}{T_{\text{dur,out}}/P_{\text{out}}^{1/3}}. \quad (\text{D5})$$

The RHS ratio is particularly useful for planetary transits as it is composed of well-measured variables. Setting the RHS to ξ (Steffen et al. 2010):

$$\xi = \frac{T_{\text{dur,in}}/P_{\text{in}}^{1/3}}{T_{\text{dur,out}}/P_{\text{out}}^{1/3}}. \quad (\text{D6})$$

From D5, a coplanar planetary pair will only give $\xi = 1$ if the invariable plane (Fig. A1) is exactly edge-on to the observer. For inclined invariable planes, a coplanar planetary pair will give $\xi > 1$, as $b_{\text{out}} > b_{\text{in}}$. Values of $\xi < 1$ are due to $b_{\text{out}} < b_{\text{in}}$, and are not possible in cases of perfect coplanarity.

APPENDIX E: PREVIOUS COPLANARITY STUDIES

⁵ Although our simulated systems may produce exactly two planets within our parameter space, we cannot rule out the possibility of additional planets outside of our parameter space, which would invalidate the analytic solution.

Table E1. Comparison of exoplanet coplanarity studies.

Reference	$\Delta\phi$ distribution	Observables	Dispersion ^a	Sample (quarter, multiplicity)	Planet sample			Dichotomy ^g
					Period (d)	Radius (R_{\oplus})	Stellar sample	
Lissauer et al. (2011)	Rayleigh	\hat{N}_k^b	$\sigma_{\phi} \sim 2.0^{\circ}$	Kepler (Q2, 1–6)	3–125	1.5–6	FGK dwarfs	2.8
Tremaine & Dong (2012)	Fisher	\hat{N}_k	$\sigma_{\phi}^c < 4.0^{\circ}$	RV and Kepler (Q2, 1–6)	<200	<22	FGK dwarfs	—
Figueira et al. (2012)	Rayleigh	\hat{N}_k	$\sigma_{\phi}^d \sim 1.4^{\circ}$	HARPS and Kepler (Q2, 1–3)	<50	>2	FGK dwarfs	—
Fang & Margot (2012)	Rayleigh, R of R	\hat{N}_k, ξ^e	$\sigma_{\phi}^c \sim 1.4^{\circ}$	Kepler (Q6, 1–6)	<200	1.5–30	FGK dwarfs	1
Johansen et al. (2012)	uniform i + rotation ^f	\hat{N}_k	$\sigma_{\phi} < 3.5^{\circ}$	Kepler (Q6, 1–3)	<240	<22	FGK dwarfs	3
Weissbein, Steinberg & Sari (2012)	Rayleigh	\hat{N}_k	No fit	Kepler (Q6, 1–6)	<75 ^h	—	FGK dwarfs	—
Hansen & Murray (2013)	Rayleigh	\hat{N}_k	—	Kepler (Q6, 1–6)	<1.1 au	—	—	2
Fabrycky et al. (2014)	Rayleigh	ξ	$\sigma_{\phi} \sim 1.8^{\circ}$	Kepler (Q6, 1–6)	<130 ^h	—	FGK dwarfs	—
Ballard & Johnson (2016)	Rayleigh	\hat{N}_k	$\sigma_{\phi} = 2.0^{\circ+4.0}_{-2.0}$	Kepler M dwarfs (Q16, 1–5)	1–200	—	M stars	3
Gaidos et al. (2016)	Rayleigh	\hat{N}_k	$\sigma_{\phi} \sim 0^{\circ}$	Kepler M dwarfs (Q16, 1–5)	<180	1–4	M stars	—
This paper	Rayleigh/flat disc	\hat{N}_k, ξ	$1.6^{+0.6}_{-0.3}$	Kepler (Q16, 1–6)	3–200	1–5	FGK dwarfs	—

Notes. ^aThe mode of the Rayleigh distribution of ϕ values (Fig. A1) around the invariable plane.

^b \hat{N}_k is the multiplicity vector for the numbers of observed k -planet systems, i.e. $\hat{N}_k = [\hat{N}_1, \hat{N}_2, \hat{N}_3, \dots]$.

^cConverted from the mean μ of the mutual inclination Rayleigh distribution: $\sigma_{\phi} = \sqrt{2/\pi} \sigma_i$.

^dConverted from Rayleigh distribution relative to the invariable plane: $\sigma_{\phi} = \sqrt{2} \sigma_{\Delta\theta}$.

^e ξ is the normalized transit duration ratio (Appendix D) as given in Steffen et al. (2010).

^fEach planet is given a random uniform inclination between 0° and 5° . This orbital plane is then rotated uniformly between 0 and 2π to give a random longitude of ascending node.

^gThe factor by which the number of simulated 1-planet systems are lower than observed.

^hConverted from a maximum semimajor axis, assuming a Solar mass star.

This paper has been typeset from a $\text{\TeX}/\text{\LaTeX}$ file prepared by the author.